# UC Santa Cruz

## UC Santa Cruz Previously Published Works


### Title

Electronic Structure, Optoelectronic Properties, and Photoelectrochemical Characteristics of γ-Cu3V2O8 Thin Films


### Permalink

https://escholarship.org/uc/item/1gv0h33j



### Journal

Chemistry of Materials, 29(7)

### ISSN

0897-4756



### Authors

Jiang, Chang-Ming
Farmand, Maryam
Wu, Cheng Hao
et al.



### Publication Date

2017-04-11

### DOI

10.1021/acs.chemmater.7b00807

Peer reviewed



eScholarship.org Powered by the California Digital Library
University of California

CHEMISTRY OF MATERIALS

Article

pubs.acs.org/cm

# Electronic Structure, Optoelectronic Properties, and Photoelectrochemical Characteristics of $\gamma$-$Cu_3V_2O_8$ Thin Films

Chang-Ming Jiang,[†,‡] Maryam Farmand,[†,‡] Cheng Hao Wu,[§] Yi-Sheng Liu,[§] Jinghua Guo,[§] Walter S. Drisdell,[†,‡] Jason K. Cooper,*[,†,‡] and Ian D. Sharp*[,†,‡]

[†]Chemical Sciences Division, [‡]Joint Center for Artificial Photosynthesis, and [§]Advanced Light Source, Lawrence Berkeley National Laboratory, Berkeley, California 94720, United States

Supporting Information

**ABSTRACT:** Thin films of n-type $\gamma$-$Cu_3V_2O_8$ are prepared with high phase purity via reactive co-sputtering deposition. Complementary X-ray spectroscopic methods are used to reveal that the valence band maximum consists of O 2*p* states, while the conduction band minimum is primarily composed of Cu 3*d* states. Therefore, $\gamma$-$Cu_3V_2O_8$ is classified as a charge transfer insulator, in which the 1.80 eV indirect band gap corresponds to the O 2*p* → Cu 3*d* transition. Through photoelectrochemical measurements, the surface of $\gamma$-$Cu_3V_2O_8$ photoanodes is found to display intrinsic activity for catalyzing water oxidation that is stable with time. The combination of a small optical band gap, suitable valence band energy, and excellent photoelectrochemical stability suggests that $\gamma$-$Cu_3V_2O_8$ could be a promising photoanode material. However, it is found that the charge extraction efficiency from these semiconductor photoanodes is strongly limited by a short (20−40 nm) hole diffusion length. Characterization of the electronic structure and transport properties of $\gamma$-$Cu_3V_2O_8$ photoanodes suggests strategies for improving energy conversion efficiency and provides fundamental insights that can be used for understanding and evaluating function in a broader class of emerging ternary metal oxides.

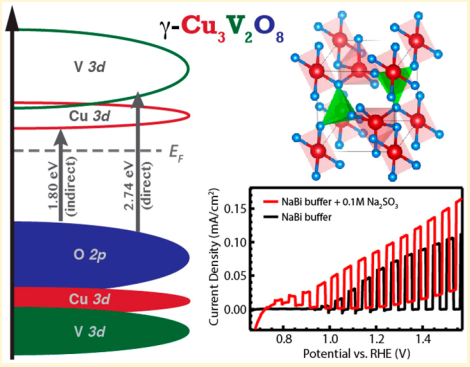


## 1. INTRODUCTION

In the pursuit of efficient solar-to-fuel conversion systems, semiconducting transition metal oxides (TMOs) have been extensively investigated as photoelectrode materials because of their potential for low-cost fabrication and chemical stability.[1−7] For driving the four proton/four electron oxygen evolution reaction (OER), various *n*-type binary TMOs have been explored and found to exhibit moderate photoelectrochemical (PEC) activity. However, the functional performance characteristics of these materials are often limited by basic optoelectronic properties of the semiconductor such as small minority charge carrier mobilities (e.g., $\alpha$-$Fe_2O_3$) or large optical band gaps (e.g., $TiO_2$ and $WO_3$).[7,8] While intensive efforts have been dedicated to addressing these challenges with novel approaches, including decoupling of the carrier diffusion length from the absorption depth via nanostructuring[9,10] and reducing the absorption onset via band gap engineering,[11] research efforts are increasingly targeting ternary metal oxides as candidate photoanode materials. A representative example of this class of materials is monoclinic bismuth vanadate (*m*-$BiVO_4$), which enables visible light absorption with a bandgap ($E_g$) of 2.5 eV and an impressive 6.72 mA/cm$^2$ photocurrent density under 1 sun illumination at 1.23 V versus the reversible hydrogen electrode (RHE).[12] Nevertheless, its bandgap remains too large to support high efficiency solar energy conversion, and new materials must be developed if a practical system is to be realized.

From the perspective of electronic structure, the band gap of $d^0$ binary oxides (e.g., $TiO_2$, $V_2O_5$, and $WO_3$) is usually dictated by transitions between O 2*p* and metal *d* states, from which the valence band maximum (VBM) and the conduction band minimum (CBM) are formed, respectively. Incorporating an open *d*-shell transition metal into these binary oxides could enable additional charge transfer pathways that lead to enhanced visible light absorption. For instance, hybridization between Cu 3*d* and O 2*p* states shifts the valence band of $CuWO_4$ upward, such that the 2.6 eV bandgap of the binary material (i.e., $WO_3$) is reduced to 2.3 eV in the ternary compound.[13] The same concept can be applied to understand the electronic structures of a series of transition metal vanadates ($M_xV_yO_z$, M = Mn, Fe, Ni, or Cu) that all possess the ability to drive photoelectrochemical oxidation reactions.[14−18] When compared to the aforementioned *m*-$BiVO_4$, these vanadate materials tend to exhibit narrower bandgaps and improved stability under long-term illumination in aqueous electrolyte, but substantially lower photocurrent densities. The present work specifically investigates the optical properties and electronic structure of $\gamma$-$Cu_3V_2O_8$ (McBirneyite), one of several possible copper vanadate (CVO) phases, as well as its PEC characteristics. Previously, Seabold and Neale showed that

Received: February 24, 2017
Revised: March 20, 2017
Published: March 21, 2017

ACS Publications © 2017 American Chemical Society



DOI: 10.1021/acs.chemmater.7b00807
Chem. Mater. 2017, 29, 3334−3345

nanocrystals of $\gamma$-$Cu_3V_2O_8$ exhibit near 100% Faradaic efficiency for $O_2$ evolution,[17] and Guo et al. reported two other CVO phases, $CuV_2O_6$ and $Cu_2V_2O_7$, as promising photoanode materials that provide 25−35 $\mu A/cm^2$ photocurrent densities at 1.23 V versus RHE.[18] By using a combinatorial synthesis approach and high-throughput characterization techniques, Zhou et al. navigated through the complicated CVO phase map and identified $\gamma$-$Cu_3V_2O_8$ to possess the highest PEC activity and stability in pH 9 borate buffer.[19]

The crystal structure of $\gamma$-$Cu_3V_2O_8$ consists of $VO_4$ tetrahedra and two distinct Cu motifs (square-planar $CuO_4$ and square-pyramidal $CuO_5$). The formal oxidation states for Cu ($3d^9$), V ($3d^0$), and O ($2p^6$) are +2, +5, and −2, respectively. The projected density of states (DOS) calculated by prior density functional theory (DFT) suggested that the conduction band edge is composed of primarily the unoccupied Cu 3*d* states, while empty V 3*d* states are located ∼1 eV higher in the CB.[19] The computed 2.05 eV indirect band gap is therefore predicted to be a charge transfer excitation from O 2*p* to Cu 3*d*. To our best knowledge, however, no experimental studies have yet verified these computational results or explored their implications on the characteristics of functional photoanodes. Here, large-scale thin films of $\gamma$-$Cu_3V_2O_8$ are prepared by reactive magnetron co-sputtering. Tauc analysis yields an indirect band gap at 1.80 eV, just slightly lower than the computational value. A weak absorption peak at 1.30 eV is assigned to localized, on-site ligand field excitations at the $Cu^{2+}$ cations ($d^9$ configuration) that do not generate conducting charge carriers. The electronic band structure of $\gamma$-$Cu_3V_2O_8$ is studied by a series of core-level spectroscopic techniques including X-ray photoemission spectroscopy (XPS), X-ray absorption spectroscopy (XAS), and resonant inelastic X-ray scattering (RIXS). A high degree of hybridization is found in the valence band, with O 2*p* states dominating the band edge. Experimental measurements confirm that unoccupied Cu 3*d* states lie near the CBM. Onsets of photoanodic current are measured at 0.85 and 0.70 V versus RHE for water and sulfite oxidation, respectively. However, it is found that the photocurrent density of $\gamma$-$Cu_3V_2O_8$ is limited by the imbalance between the large absorption depth, $\alpha^{-1}$, and the short hole diffusion length, $L_h$. Findings of the present work provide fundamental insights into how the electronic structure and optoelectronic properties of $\gamma$-$Cu_3V_2O_8$ affect its photoelectrochemical characteristics, as well as charge extraction limitations, and suggest feasible strategies for improving PEC performance. In addition, these results are expected to aid in evaluation of the broader class of emerging transition metal vanadates as candidates for next generation photoanodes.

## 2. EXPERIMENTAL SECTION

**2.1. Preparation of $\gamma$-$Cu_3V_2O_8$ Thin Films.** Thin films of $\gamma$-$Cu_3V_2O_8$ were grown by radio frequency magnetron co-sputtering of Cu and V metal targets onto 25 × 75 $mm^2$, 1.1 mm thick indium tin oxide (ITO) coated glass substrates (CB-40IN-S111, Delta Technologies) in a sputtering deposition system (LAB Line, Kurt J. Lester). The reactive working atmosphere consisted of 10 mTorr of inert Ar and 1 mTorr of $O_2$, and the substrate temperature was kept at 450 °C during the process. The powers on the metal targets were 31 and 260 W for Cu and V, respectively, which translated to a growth rate of ∼4 nm/min. The as-deposited films were then annealed in air at 550 °C for 1 h with a 12 °C/min ramp rate, followed by natural cooling to room temperature, using a box furnace (CBFM518C, Cole Parmer). A series of films with seven different thicknesses (25−1200 nm) was prepared by varying the sputtering time between 6 and 300 min. We note that annealing of ITO to 550 °C can yield increased resistivity. Tests on bare ITO, unprotected by a CVO overlayer, reveal an increase of resistivity from ∼30 to ∼100 Ω/cm, which has little impact on observed photoelectrochemical characteristics due to the low photocurrent densities measured in this work. To enable ellipsometric study of the material, a 500 nm thick $\gamma$-$Cu_3V_2O_8$ film was grown on a 1 mm thick quartz substrate (Chemglass) following the identical procedures and conditions.

**2.2. Material Characterization.** The crystalline structures of CVO thin films were analyzed by grazing incidence X-ray diffraction (GIXRD) with a Rigaku Smartlab diffractometer using Cu−$K_\alpha$ radiation. The incident angle, $\omega$, was fixed at 0.5°, and the detector angle, $2\theta$, was scanned between 10 and 70° with 0.02° intervals. Sample morphologies were inspected at the sub-$\mu$m scale using a scanning electron microscope (Quanta FEG 250, FEI) with a 10 kV acceleration voltage and a 10 mm working distance. Stoichiometric composition was obtained by an inductively coupled plasma mass spectrometer (7900 ICP-MS, Agilent) after CVO thin films were dissolved in concentrated nitric acid. Raman spectra were recorded using a confocal Raman microscope (LabRam HR, Horiba Jobin Yvon) with a 532 nm laser source. The excitation laser power at the sample surface was adjusted to be in the 1−2 mW range, and the spectral positions were calibrated by the characteristic Si phonon peak at 520.7 $cm^{-1}$.

Optical properties of $\gamma$-$Cu_3V_2O_8$ thin films, including transmission and specular reflection (∼5° incident angle), were recorded using a UV−vis spectrometer equipped with an integrating sphere (SolidSpec-3700, Shimadzu) over the range from 300−900 nm. Because the UV−vis spectrometer has limited photon flux in the infrared region, variable angle spectroscopic ellipsometry (VASE) was used as a parallel technique for extracting the absorption coefficient: the changes in intensity and polarization of incident light ($\lambda$ = 193−1690 nm) after interacting with the target thin film were recorded by an ellipsometer (M-2000DI, J. A. Woollam Co.) as a function of incident angle between 45 and 75° with 5° increments.

X-ray photoelectron spectroscopy (XPS) data were acquired by a Kratos Axis Ultra spectrometer, using an Al−$K_\alpha$ source ($h\nu$ = 1486.69 eV) operated at 225 W and a hemispherical electron energy analyzer. A −10 V bias voltage was applied during the measurement of work function. Spectral fitting was conducted using CasaXPS software. Following Shirley background subtraction, the acquired core-level spectra (O 1*s*, V 2*p*, and Cu 2*p*) were fit with quasi-Voigt functions. Spectral positions were calibrated using adventitious alkyl carbon signals by shifting the C 1*s* peak to 284.8 eV.

X-ray absorption spectroscopy (XAS) measurements of the O K-edge, Cu L-edge, and V L-edge were performed at beamline 6.3.1 of the Advanced Light Source (ALS) at Lawrence Berkeley National Laboratory (LBNL). A variable line spacing plane-grating monochromator was used for controlling the incident photon energy with <150 meV energy resolution, and the absorption data were collected simultaneously in the total electron yield (TEY) and the total fluorescence yield (TFY) modes, which both gave very similar results. The acquired XAS spectra were normalized to the incident photon flux monitored by measuring the photocurrent from a gold mesh upstream in the beamline. Energy calibration at O K-edge (plus the neighboring V L-edge) and Cu L-edge was done with $TiO_2$ and CuO standards, respectively.

Nonresonant X-ray emission spectroscopy (XES) and resonant inelastic X-ray scattering (RIXS) data were collected at beamline 8.0.1 of the ALS using a Rowland-circle grating spectrometer equipped with a two-dimensional multichannel plate detector with ∼400 meV instrument resolution. The monochromator resolution for X-ray excitation was ∼150 meV at the O K-edge. The emission energy was calibrated using the positions of the elastic scattering peak in the emission spectra.

**2.3. Photoelectrochemical (PEC) Measurements.** The PEC measurements were conducted using an AM1.5 solar simulator (16S-300−002, Solar Light) in a three-electrode configuration. The $\gamma$-$Cu_3V_2O_8$ thin film and a Pt wire served as the working and counter


DOI: 10.1021/acs.chemmater.7b00807
Chem. Mater. 2017, 29, 3334−3345

electrode, respectively, while a Ag/AgCl electrode immersed in 3 M KCl solution was used as the reference electrode. The pH 9.2 buffer solution consisted of 0.1 M $H_3BO_3$ (Sigma-Aldrich) and 0.05 M NaOH (Sigma-Aldrich), with the option of adding 0.1 M $Na_2SO_3$ (Alfa Aesar) as a sacrificial hole acceptor. Current−voltage characteristics were recorded with a potentiostat (SP-300, Bio-Logic), and the reported potentials were converted to the reversible hydrogen electrode (RHE) scale using the following relation:

$$E_{RHE} = E_{Ag/AgCl} + 0.210\ V + (0.0591\ V \times pH) \quad (1)$$

The incident photon-to-current efficiency (IPCE) was measured in pH 9.2 borate buffer with the presence of 0.1 M $Na_2SO_3$ at 1.23 V versus RHE external bias. A 150 W Xe arc lamp (M6255, Newport) combined with a holographic grating monochromator (CS-130, Oriel Instruments) was used to illuminate the front-side of the $\gamma$-$Cu_3V_2O_8$ sample in a PEC cell, while differences in photocurrent and dark current responses at individual wavelength were acquired by a Gamry Reference 600 potentiostat. The reference incident spectrum was measured by recording the photocurrent response from a calibrated Si photodiode at 10 nm intervals between 290 and 800 nm.

## 3. RESULTS AND DISCUSSION

Copper vanadate (CVO) thin films deposited by reactive co-sputtering exhibited a homogeneous reddish−brown color over the entire 25 × 75 $mm^2$ substrate after 1 h of post deposition air annealing at 550 °C. Depending on the elemental Cu/V ratio of the deposited films, which was tunable by varying the sputtering powers on the Cu and V targets, several CVO phases could be accessed, as determined by grazing incidence XRD (GIXRD) and shown in Figure S1 of the Supporting Information. In the sequence of Cu-rich to V-rich phases, the identified phases in the different films were $Cu_5V_2O_{10}$ (Stoiberite), $Cu_{11}V_6O_{26}$ (Fingerite), $\gamma$-$Cu_3V_2O_8$ (McBirneyite), and $\beta$-$Cu_2V_2O_7$ (Ziesite). The GIXRD pattern of the $\gamma$-$Cu_3V_2O_8$ film, which is the focus of this study, is shown in Figure 1a and indicated that the film is of very high phase purity, with the diffraction peak at $2\theta$ = 24.7° caused by the presence of trace amount $\beta$-$Cu_2V_2O_7$, the coexistence of which was also observed in a previous combinatorial study.[19] The Raman spectrum from our sputtered $\gamma$-$Cu_3V_2O_8$ exhibited scattering peaks at ~860 and 920 $cm^{-1}$ that are associated with tetrahedral $VO_4$ stretching modes, along with peaks at 380 and 545 $cm^{-1}$ that are due to the bending of the same structural motif (Figure S2).[20] The stoichiometric transition metal ratio, Cu/(Cu+V), of films dissolved in $HNO_3$ was analyzed by ICP-MS. The ratio of 0.602 ± 0.012, averaged from measurement of seven films of different thicknesses, agrees well with the expected value of 0.600 for $\gamma$-$Cu_3V_2O_8$. The SEM image (Figure 1b) shows that the grains are approximately 100−300 nm in size and form a homogeneous layer on the substrate. In comparison with previously reported films prepared from nanocrystals,[17] thin films deposited by reactive co-sputtering exhibit a significantly more compact morphology. In addition to precise composition control and excellent reproducibility, the reactive co-sputtering method presented in this work provides potential for scale-up and integration with other components in future solar fuels devices.

The transmittance and specular reflectance curves of a 200 nm $\gamma$-$Cu_3V_2O_8$ thin film are shown in Figure 2a. Although the transmission dropped sharply at approximately 600 nm, an optical band gap cannot be precisely assigned since both response functions are convoluted with interference oscillations. The absorption coefficient, $\alpha$, was therefore calculated using the following equation:

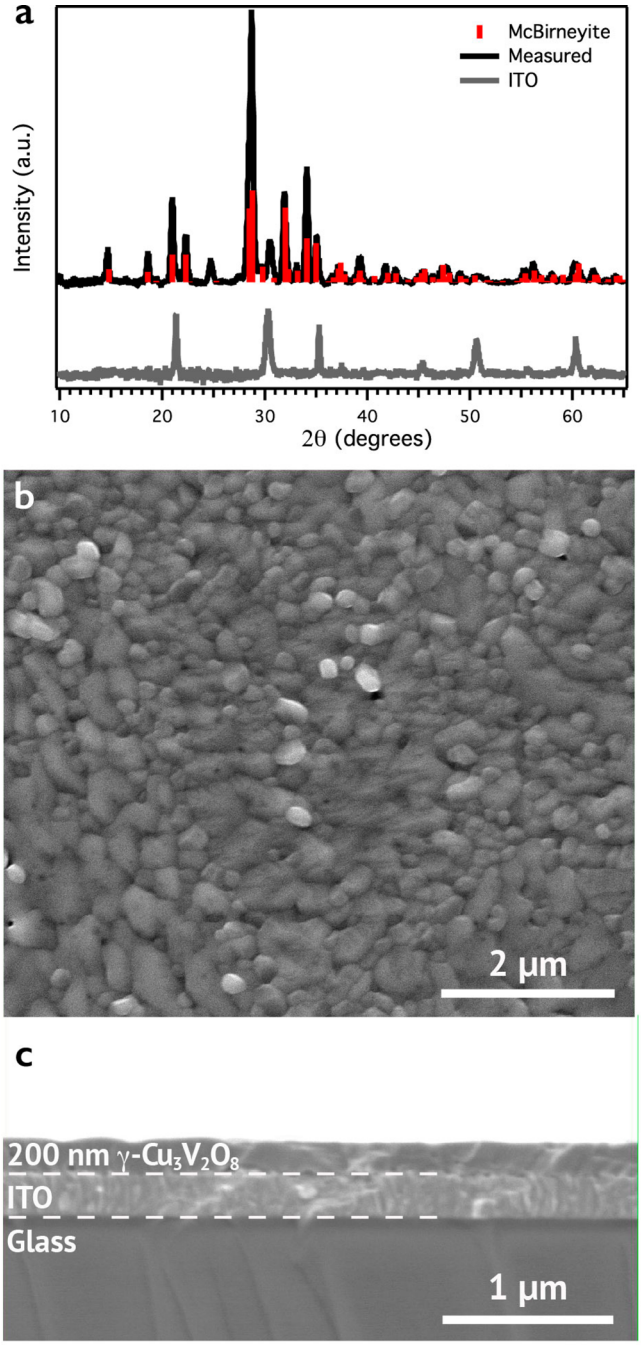


**Figure 1.** (a) GIXRD pattern measured from a sputtered $\gamma$-$Cu_3V_2O_8$ thin film (black), compared to the measured pattern from the ITO substrate (gray) and the reference peak positions of McBirneyite (red lines, ICSD #04−010−1734). (b) Plane view and (c) cross-sectional SEM images of a 200 nm $\gamma$-$Cu_3V_2O_8$ thin film deposited on an ITO-coated glass substrate.

$$\alpha = -\ln[(\%T + \%R)/100]/d \quad (2)$$

where $d$ is the film thickness determined by cross-sectional SEM. Linear regions in Tauc plots (Figure 2b) indicate that the indirect and direct allowed band gaps are 1.80 and 2.74 eV, respectively. Weak optical absorption below the 1.80 eV band gap can be seen in the indirect allowed Tauc plot. A similar feature has also been observed, but not assigned, for a variety of CVO phases measured in a previous high-throughput study.[19] To better resolve this absorption feature in the near-infrared



DOI: 10.1021/acs.chemmater.7b00807
Chem. Mater. 2017, 29, 3334−3345

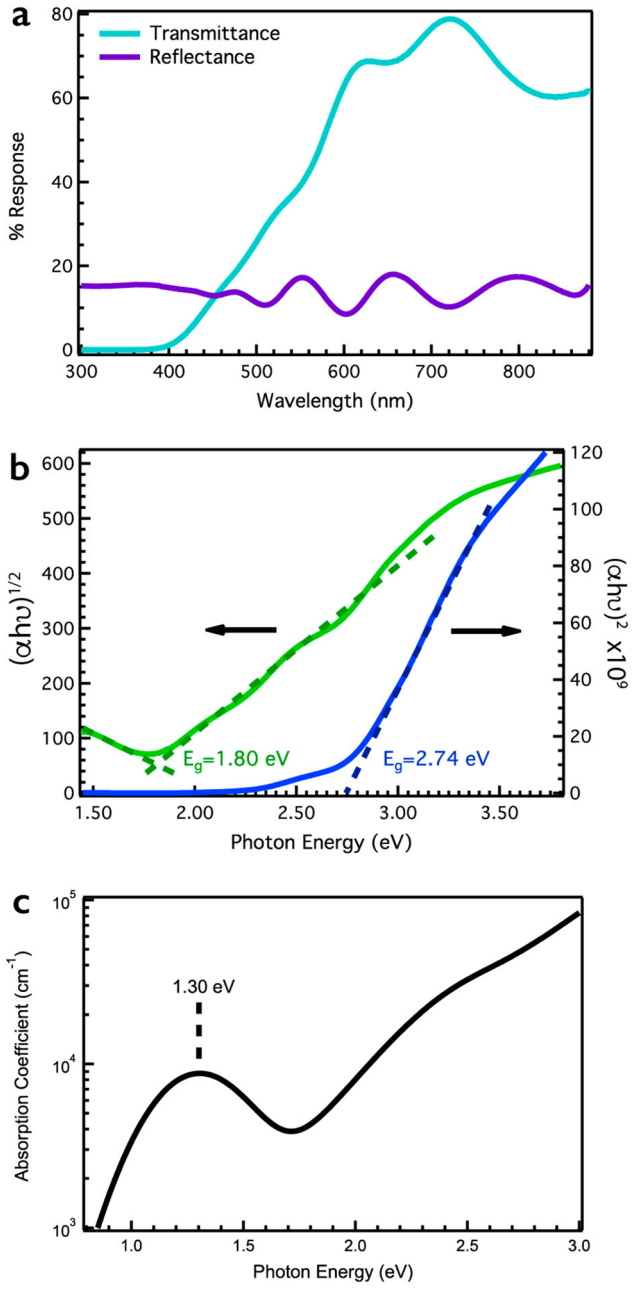


**Figure 2.** (a) Transmission (cyan) and reflection (purple) spectra of a 200 nm $\gamma$-$Cu_3V_2O_8$ film on an ITO-coated glass substrate, measured with an integrating sphere as a function of wavelength. (b) Tauc plots for indirect (green) and direct (blue) allowed transitions. (c) Absorption coefficient, $\alpha$, of $\gamma$-$Cu_3V_2O_8$ measured by VASE, plotted as a function of photon energy.

region, variable angle spectroscopic ellipsometry (VASE) was performed on a $\gamma$-$Cu_3V_2O_8$ thin film deposited on a quartz substrate (Figure S3). In the visible wavelength region, the absorption coefficient measured by VASE (Figure 2c) is close to the UV−vis result, and the $10^3$−$10^4$ $cm^{-1}$ magnitude of $\alpha$ is similar to that of other indirect band gap oxides.[21,22] In the sub-bandgap range, a symmetric absorption peak centered at 1.30 eV was also observed. A likely origin of this absorption feature is the local ligand field excitations of $Cu^{2+}$ cations: the open *d*-shell of $Cu^{2+}$ ($3d^9$) allows on-site excitations of *d*-shell electrons into the half-filled Cu $d_{x^2-y^2}$ orbital within both the square-planar $CuO_4$ and the square-pyramidal $CuO_5$ motifs. In other $Cu^{2+}$-containing oxides, such as CuO and $CuWO_4$, a similar weak absorption peak can be seen below 1.5 eV (or at wavelengths >800 nm).[13,23,24] In contrast, such a ligand field-induced optical absorption feature is not present in $Cu^+$-based oxides (e.g., $Cu_2O$ and $CuMnO_2$) because the Cu 3*d* shell is completely full.[25,26]

XPS analysis was used to evaluate the chemical and electronic properties of $\gamma$-$Cu_3V_2O_8$. The O 1*s*, V 2*p*, and Cu 2*p* core level XPS spectra, shown in Figure 3, are in agreement with the expected formal oxidation states of these elements in the material. In particular, the 516.87 eV binding energy of the sharp V $2p_{3/2}$ peak (Figure 3a) is close to the reported value of $V_2O_5$ and indicates $V^{5+}$ as the dominant oxidation state.[27] The O 1*s* spectrum contains two primary components (Figure 3b), with the peak at 530.13 eV consistent with lattice $O^{2-}$ and the higher binding energy contribution near 532 eV arising from adsorbed water or surface oxygen-bearing groups. As shown in Figure 3c, the binding energy of the broad Cu $2p_{3/2}$ peak (934.33 eV), together with the strong satellite peaks in the range of 940−945 eV, indicates that $Cu^{2+}$ is the dominant oxidation state.[28−30] Fitting parameters for the Cu $2p_{3/2}$ XPS spectrum (including peak position, peak width, and underlying area for each component) are listed in Table S1, and a weak component at 931.69 eV, associated with the presence of $Cu^+$, is observed. Quantitative analysis indicates ∼3% of the Cu atoms were reduced to the +1 oxidation state. This presence of $Cu^+$ may provide the source of native *n*-type doping in the films, which is indicated by the valence band spectrum (Figure 3d) in which the onset of photoemission occurs at 1.46 eV below the Fermi energy ($E_F$); the fact that $E_F$ is located closer to the CBM than VBM confirms the sputtered $\gamma$-$Cu_3V_2O_8$ to be an *n*-type semiconductor. The position of $E_F$ was found to be 4.57 eV below the vacuum level by photoemission-based work function measurements (Figure S4). Hence, the energetic positions of the VBM and CBM are located at 6.03 and 4.23 eV below the vacuum level, respectively (using the 1.80 eV indirect band gap).

Additional insight into the electronic structure of $\gamma$-$Cu_3V_2O_8$ is obtained by comparing XPS data collected in darkness and under optical excitation. As shown in Figure 3c, the intensity of the $Cu^+$ component increased significantly when the sample was illuminated with a 405 nm laser diode (CPS405, Thorlabs). The observation of a significant increase in the $Cu^+$ contribution under illumination suggests that the CBM is composed of Cu 3*d* states. Furthermore, this formal oxidation state change may indicate electron localization at Cu sites, which is characteristic of small electron polaron formation. A similar oxidation state change from $V^{5+}$ to $V^{4+}$ has been previously reported for photocharged $BiVO_4$,[31] in which the CBM mainly consists of V 3*d* states.[32] It should be noted that XPS is a surface-sensitive technique; therefore, the observation of additional $Cu^+$ under light illumination may not reflect the response from the bulk $\gamma$-$Cu_3V_2O_8$. The results of RIXS measurement, which is a bulk-sensitive technique, will verify the findings of XPS analysis, as discussed in later paragraphs.

To compliment photoemission measurements, which provide a measure of occupied states in the material, X-ray absorption spectroscopy (XAS) was used to probe the unoccupied states in the conduction band. X-ray absorption at metal (Cu and V) L-edges promotes 2*p* electrons into unoccupied 3*d* levels, but the measured spectra are dominated by the spin−orbit effects and thus do not resemble the element-specific DOS (Figure S5). On the other hand, because of


DOI: 10.1021/acs.chemmater.7b00807
Chem. Mater. 2017, 29, 3334−3345

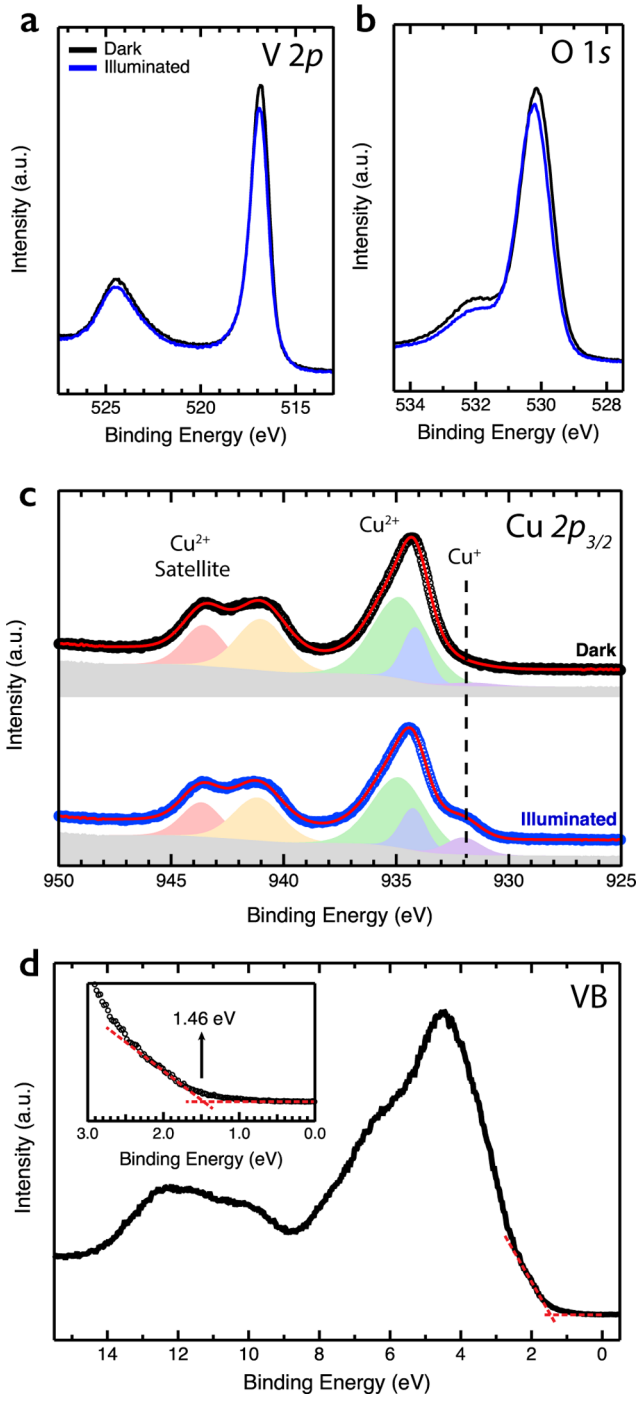


**Figure 3.** (a) O 1*s*, (b) V 2*p*, and (c) Cu $2p_{3/2}$ XPS spectra of a $\gamma$-$Cu_3V_2O_8$ thin film acquired in dark condition (black) and under the illumination of a 405 nm laser diode (blue). Cu $2p_{3/2}$ fitting results, which are the sum over a Shirley background (gray) and five quasi-Voigt components, are shown in red lines. (d) Valence band XPS spectrum acquired in dark condition. Inset: the enlarged region showing the valence band onset.

hybridization with Cu 3*d* and V 3*d* orbitals, O K-edge XAS, which probes the O 1*s* → O 2*p* transitions, allows characterization of orbitals containing O 2*p* antibonding character in the conduction band, manifested by the absorption features in the energy range 528−535 eV in Figure 4a, without spin−orbit effects. We note that first-principles calculations of electronic structure and associated XAS spectra could provide additional insights into *d*-manifold splitting and local coordination structures around $Cu^{2+}$ and $V^{5+}$, but such calculations are beyond the scope of the present work. Nevertheless, experimental XAS spectra provide powerful information about the electronic structure of the material. As shown in Figure 4a, the O K-edge XAS spectrum of $\gamma$-$Cu_3V_2O_8$ contains two peaks at 529.9 and 531.5 eV. Previously, a similar dual-peak feature (at 529.6 and 531.0 eV) was seen in $BiVO_4$, in which the CBM mainly consists of V 3*d* states.[32] In comparison, only a single peak at 530.1 eV was observed in a prior study reporting O K-edge XAS of CuO thin films.[29] The dual-peak feature in $BiVO_4$ has been attributed to the *d*-manifold splitting due to the distortion of $VO_4$ tetrahedra.[32] Close inspection reveals the difference in relative intensities of the two peaks at the O K-edge: in $\gamma$-$Cu_3V_2O_8$, the amplitude of the 529.9 eV peak is larger than that of the 531.5 eV peak, but in $BiVO_4$, the 531.0 eV peak is more intense than that of the 529.6 eV peak. While unoccupied Bi 6*p* states are found to be 3 eV higher than the CBM in $BiVO_4$, the unoccupied Cu 3*d* states in $\gamma$-$Cu_3V_2O_8$ are expected to be near the band edge according to XPS results (see above) and DFT calculations.[19] The additional unoccupied states observed at the onset of O K-edge XAS in $\gamma$-$Cu_3V_2O_8$, as compared to $BiVO_4$, are consistent with the assignment of Cu 3*d* states at the bottom of the conduction band.

We now return to characterization of the VB electronic structure. While X-ray photoemission spectra from the VB region provide information about occupied states near band-edge, spectral contributions are fixed by elemental photo-ionization cross-sections at the single excitation energy. However, nonresonant X-ray emission spectroscopy (XES) using synchrotron light sources can be used for qualitatively deconvoluting the partial densities of states (pDOS) in the valence band contributed by different elements: following absorption of X-ray photons with energy much higher than the specific XAS edge of the investigated elemental transition, the core hole recombines with a valence electron, which results in the emission of an X-ray photon containing information about the element-specific states comprising the valence band. In Figure 4b, the O $K_\alpha$, Cu $L_\alpha$, and V $L_\alpha$ emission spectra are plotted on a common energy scale by aligning the leading spectral edges to an arbitrary Fermi level $E_F'$. This analysis scheme, based on leading edge energy alignment, has been successfully applied to understand the *p*-*d* hybridization in the valence bands of transition metal fluorides, of which the peaks of the F $K_\alpha$ emission align with the shoulders of metal $L_\alpha$ emission and the peaks of metal $L_\alpha$ emission align with the shoulders of F $K_\alpha$ emission.[33] Because of the higher covalence in the oxide system, the distinction between the X-ray emission peak and shoulder is expected to be less obvious. Nevertheless, Figure 4b provides valuable insights into the relative positions of individual orbital contributions to the valence band. We note that, because of the proximity of the V L-edge to the O K-edge, the V XES spectrum in Figure 4b was measured with an excitation energy 519.14 eV that avoided interference from oxygen. With the leading edges of three spectra aligned, the broad V emission peak overlaps with the low energy shoulder of the O $K_\alpha$ spectrum, while the sharp peak of Cu $L_\alpha$ emission sits between the main peaks of O and V. Weak shoulders on the high energy side of the main peaks from both Cu and V emission spectra are observed and coincide with the main peak from the O $K_\alpha$ emission spectrum due to orbital hybridization. Therefore, in the sequence of higher to lower energy, the


DOI: 10.1021/acs.chemmater.7b00807
*Chem. Mater.* 2017, 29, 3334−3345

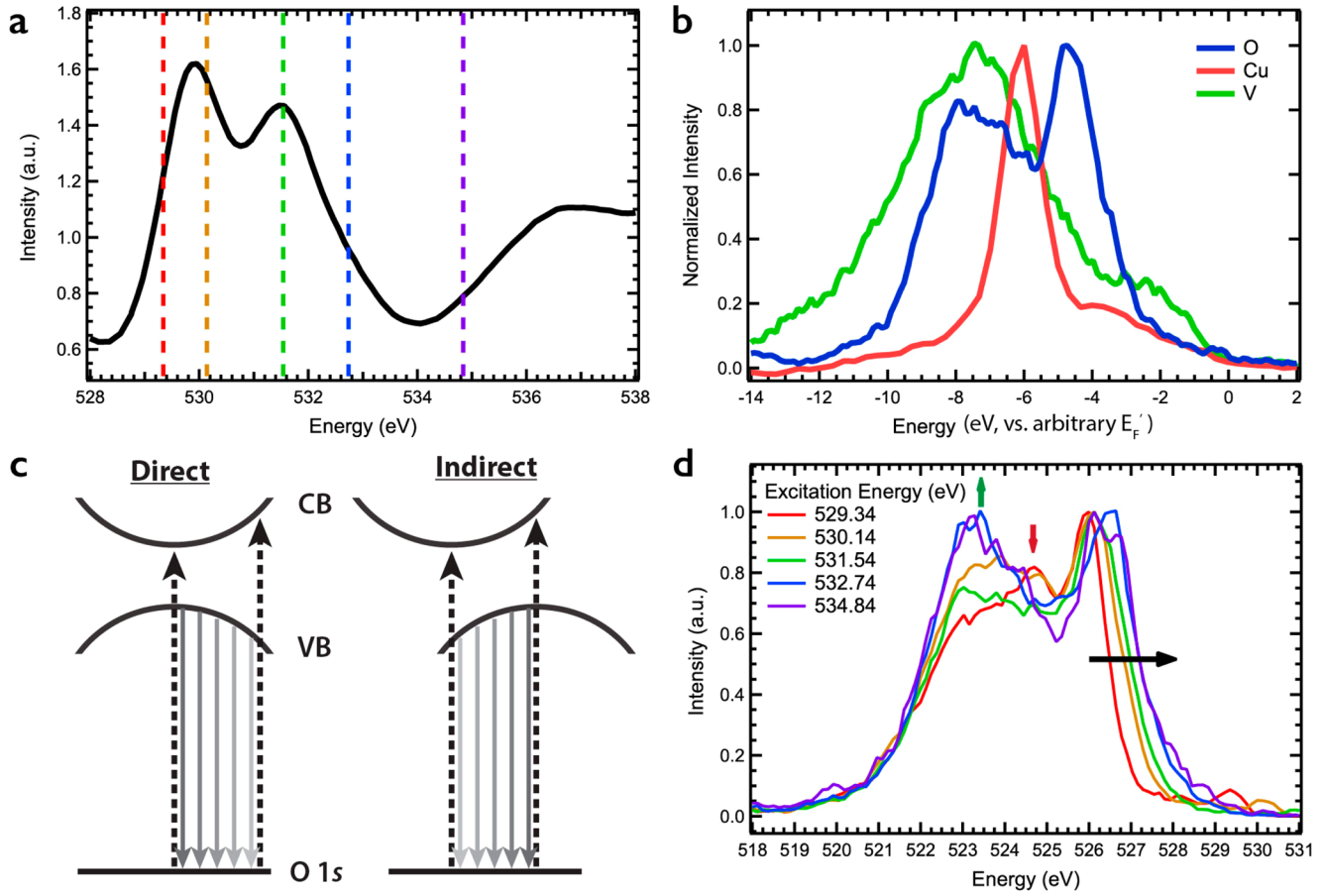


**Figure 4.** (a) O K-edge XAS spectrum of $\gamma$-$Cu_3V_2O_8$. Dashed lines indicate the excitation energies used in the RIXS experiment. (b) O $K_\alpha$ (blue) and Cu $L_\alpha$ (red) nonresonant X-ray emission spectra. Because of the overlap with O K-edge, the V L-edge XES spectrum (green) was measured with 519.14 eV excitation. The leading edges of all three spectra are aligned to an arbitrary Fermi energy $E_F'$. (c) Schematic representation illustrating the excitation energy dependence of the X-ray emission energy in RIXS measurements. (d) Resonantly excited O K-edge XES as a function of X-ray excitation energy. The horizontal black arrow indicates the blueshift with increasing excitation energy, the vertical red arrow indicates the weak peak associated with Cu *d*-orbital hybridization, and the vertical green arrow indicates the spectral region dominated by hybridization with V *d*-orbitals.

contributions to the valence band can be characterized as O 2*p*, hybridized Cu 3*d*−O 2*p* bonding states, and hybridized V 3*d*−O 2*p* bonding states, respectively. Importantly, the VBM pDOS is dominated by O 2*p* states.

RIXS[34] measurements were performed to probe the nature of band-to-band transitions and verify the spectral assignments described above. In this photon-in/photon-out technique, the incident X-ray photon resonantly promotes a core-level electron into the conduction band (instead of the vacuum level in the case of nonresonant XES); then the core hole in the intermediate state is radiatively annihilated by a valence electron. Consequently, the final state in RIXS measurements comprises an electron in the conduction band and a hole in the valence band, equivalent to the final state of an optical band gap excitation. Since the momentum of the incident X-ray photon is negligible, RIXS offers the additional advantage of probing vertical transitions in the wave-vector ($k$) space and can be used as a powerful tool for studying electronic structure[35,36] and discerning the nature of the band gap.[21] As shown schematically in Figure 4c, for the case of direct gap semiconductors, like CdO[37] and GaN,[38] the CBM and VBM are aligned in *k*-space. Therefore, X-ray excitation to the CBM yields the highest emitted X-ray photon energy, and a redshift of the emission energy occurs with increasing excitation energy. In contrast, indirect bandgap semiconductors are characterized by a blueshift of X-ray emission with increasing X-ray excitation energy, as shown schematically in Figure 4c and previously reported in $\alpha$-$Fe_2O_3$,[39] Be chalcogenides,[40] and $BiVO_4$.[21,41]

Figure 4d shows the result of O K-edge RIXS from sputtered $\gamma$-$Cu_3V_2O_8$ films. The 529.34 eV excitation marks the promotion of an O 1*s* electron into the CBM (see corresponding vertical dashed line in Figure 4a). As the X-ray excitation energy was increased and core electrons were excited to higher lying states in the CB, the leading edge of the resulting X-ray emission was observed to blueshift. This result suggests that $\gamma$-$Cu_3V_2O_8$ has an indirect band gap and is in agreement with the Tauc analysis (see above).

RIXS measurements also reveal that the spectral shape of O K-edge emission evolves with excitation energy. This effect manifests by the growth of a peak at 523.4 eV with increasing X-ray excitation energy. In addition, a smaller emission peak near 524.7 eV is only observed upon excitation near the XAS onset. These observations can be explained by simultaneously considering the nature of the states in the CB that participate in X-ray absorption and those in the VB that participate in X-ray emission. We also note that this analysis is based on O K-edge RIXS since hybridization between oxygen *p*-orbitals and the transition metal *d*-orbitals provides sensitivity across the near-band edge range. The excitation energy dependence of the 524.7 eV feature is explained by the presence of Cu 3*d* states at


DOI: 10.1021/acs.chemmater.7b00807
*Chem. Mater.* 2017, 29, 3334−3345

the CBM and in the middle of the VB, such that XES spectra associated with excitations at the O K-edge absorption onset would lead to enhanced intensity from the energetic region dominated by the pDOS of Cu in the VB. As the excitation energy moves off resonance for Cu 3*d* states in the CB, the spectral weight from this feature in the VB is reduced. Likewise, at higher excitation energies, absorption occurs to states higher in the conduction band, where unoccupied V 3*d* states dominate. As a result, the emission intensity increases in the energy range where the pDOS for V is dominant. The observed spectral shape evolution is consistent with the pDOS assignments made from analyzing nonresonant XES spectra, as discussed above and shown in Figure 4b. As shown by the vertical dashed lines in Figure 4a, excitation with 529.34 and 530.14 eV photons leads to resonant absorption to the lowest energy peak of the O K-edge absorption spectrum. The resulting emission spectra are characterized by a 1.3 eV difference between the main peak (~526.0 eV) and the weaker resonance feature (~524.7 eV), which is in good agreement with the separation between the primary peaks in the nonresonant XES of O $K_\alpha$ and Cu $L_\alpha$ when the spectral leading edges are aligned (Figure 4b). At X-ray energies of 531.54 and 532.74 eV, the excitation moved into resonance with the second O K-edge absorption peak and the weak emission peak at ~524.7 eV could no longer be resolved. This spectral change was accompanied by the appearance of a broad emission peak at 523.3 eV, which matched well the V pDOS in the valence band from the nonresonant XES analysis. Thus, the RIXS results are in excellent agreement with assignments made from both XAS and nonresonant XES measurements and confirm the different elemental contributions to the DOS in the near band-edge region of $\gamma$-$Cu_3V_2O_8$.

A schematic summary of the near band-edge electronic structure and associated optical transitions of $\gamma$-$Cu_3V_2O_8$ is presented in Figure 5. Combining experimental results from

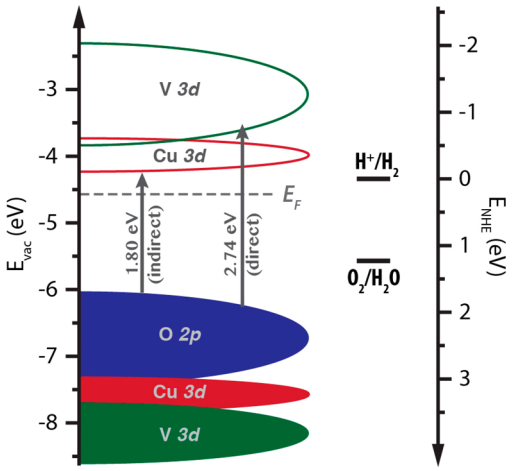


**Figure 5.** Illustration of the optoelectronic structure of $\gamma$-$Cu_3V_2O_8$ with respect to the vacuum level.

XPS, XAS, nonresonant XES, and RIXS, it is found that the VBM is mainly of O 2*p* character, with Cu 3*d* and V 3*d* contributions deeper within the VB. The unoccupied 3*d* states of $Cu^{2+}$ dominate the CBM, while the $V^{5+}$ 3*d* states dominate at higher energies within the conduction band. With these assignments, we can classify $\gamma$-$Cu_3V_2O_8$ as a charge transfer insulator in which the *d*−*d* Coulomb repulsion energy of Cu is greater than the charge transfer gap separating O 2*p* states from unoccupied transition metal 3*d* states.[42] Stated differently, the CBM comprises the upper Hubbard band arising from the highly correlated unpaired electrons of $d^9$ Cu in $\gamma$-$Cu_3V_2O_8$, while the VBM comprises the O 2*p* ligand band, with energy that is higher than the lower Hubbard band. It should be noted that the experimental findings of the present work are qualitatively consistent with the pDOS distributions predicted by previous DFT calculations.[19] The 1.80 eV indirect band gap of $\gamma$-$Cu_3V_2O_8$, which is slightly larger than the 1.4 eV value of CuO[23] but less than the reported 2.04−2.66 eV band gap of $V_2O_5$,[43] reflects the O 2*p* → Cu 3*d* charge transfer transition. It is worthwhile to compare the distinct influence of incorporating $Cu^{2+}$ into a prototypical binary $d^0$ oxide, such as $CuWO_4$, in which the valence band energy is raised by hybridization of Cu 3*d* and O 2*p* but the CBM is not affected and remains dominated by W 5*d* states.[13] In contrast, like $V_2O_5$, the VBM of $\gamma$-$Cu_3V_2O_8$ remains dominated by O 2*p* states, but the unoccupied Cu 3*d* states lower the CBM and shrink the band gap.

Figure 5 suggests that both the equilibrium HER and OER potentials (0 and 1.23 V vs RHE, respectively) are straddled by CBM and VBM, making $\gamma$-$Cu_3V_2O_8$ an energetically desirable material for water-splitting applications. However, it must be noted that the band edge energies demonstrated here are unique to the semiconductor−vacuum interface, as well as the specific nature of the surface termination under measurement conditions.[44] In a PEC system, where the semiconductor is in contact with aqueous solution, charge and chemical rearrangement at the semiconductor−liquid junction (SCLJ) would induce an additional band edge energy shift that is specific to the semiconductor and its surface chemistry. Therefore, it is necessary to measure the energy alignment, including the flat band potential, at the SCLJ by (photo)electrochemical methods. Seabold et al.[17] reported a ~0.66 eV flat band potential for an electrode made of $\gamma$-$Cu_3V_2O_8$ nanocrystals by Mott−Schottky measurements. This value was very close to the 0.70 V versus RHE photocurrent onset for the facile sulfite oxidation reaction observed in the same study. In the present work, the linear sweep voltammetry (LSV) curve of a sputtered $\gamma$-$Cu_3V_2O_8$ thin-film electrode is plotted in Figure 6a. A photocurrent density of ~62 $\mu A/cm^2$ for water oxidation was measured in the absence of sacrificial hole acceptor at 1.23 V versus RHE in the pH 9.2 buffer solution and under AM1.5 simulated solar irradiation at 1 sun intensity (100 $mW/cm^2$). The absence of photocurrent spikes as the illumination source was chopped indicates that carrier recombination through surface states was negligible. Most likely because of the overpotentials associated with water oxidation reactions, the ~0.85 V versus RHE onset potential is more anodic than the previously reported flat band potential. When 0.1 M $Na_2SO_3$ was added into the buffer solution as sacrificial hole acceptor, the photocurrent density at 1.23 V versus RHE increased by almost 50%, to ~91 $\mu A/cm^2$, and the onset potential was reduced to 0.70 V versus RHE, which is identical to the previously reported onset for sulfite oxidation.[17] Moreover, the dark current in the present work is significantly lower than from the previously reported nanocrystal films, reflecting the highly compact morphology of the $\gamma$-$Cu_3V_2O_8$ thin films prepared by the reactive co-sputtering method.

The incident photon-to-current efficiency (IPCE) spectrum was measured at an applied bias of 1.23 V versus RHE in pH 9.2 buffer solution containing $Na_2SO_3$ as sacrificial hole


DOI: 10.1021/acs.chemmater.7b00807
Chem. Mater. 2017, 29, 3334−3345

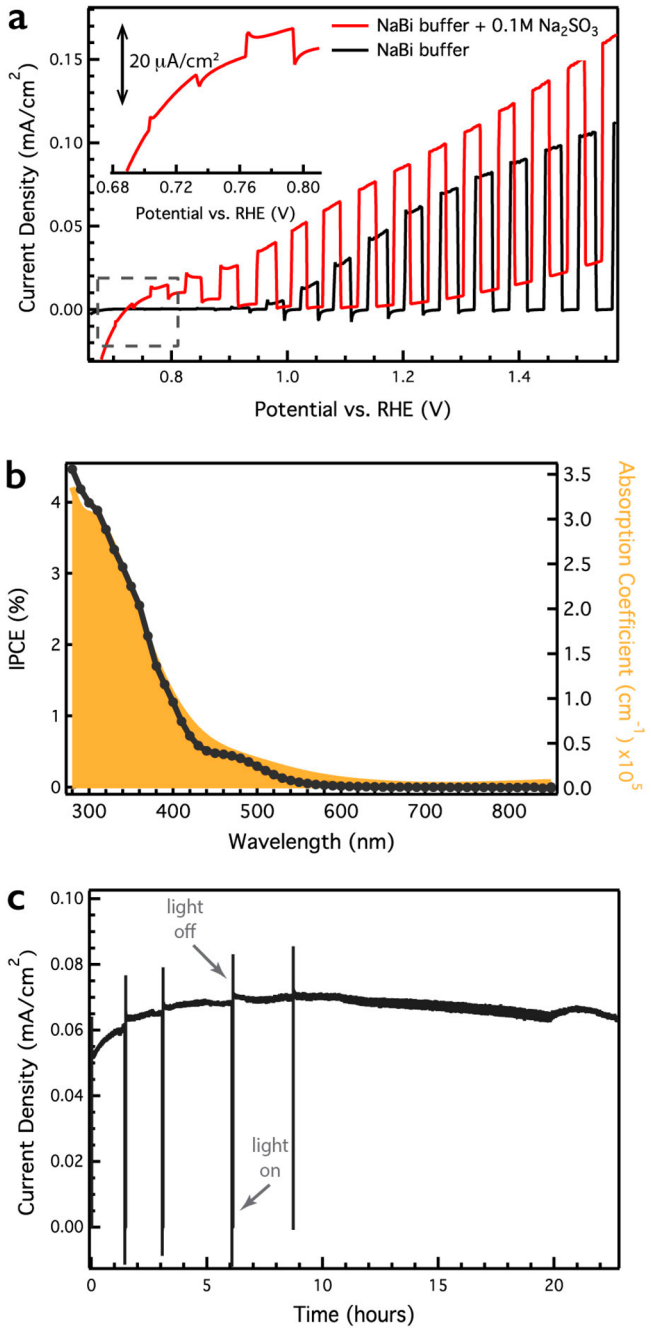


**Figure 6.** (a) Linear sweep voltammetry (LSV) measurement of a $\gamma$-$Cu_3V_2O_8$ photoelectrode under chopped front-side illumination by simulated AM1.5 irradiation at 1 sun intensity. The scan rate was 50 mV/s. (b) IPCE spectrum of $\gamma$-$Cu_3V_2O_8$ thin film at 1.23 V versus RHE. The yellow line indicates the absorption coefficient $\alpha$ obtained by VASE. (c) Chronoamperometry measurement in 0.1 M sodium borate buffer (pH 9.2) under front-side AM1.5 irradiation at 1 sun intensity and at an applied potential of 1.23 V versus RHE.

acceptor. As shown in Figure 6b, the result is in agreement with the wavelength dependence of the absorption coefficient and, within the instrumental sensitivity, the onset of photocurrent was found to be at ~600 nm, reaching 3% efficiency at 360 nm. The low IPCE responses are likely caused by poor charge carrier mobility, such that only a small fraction of photogenerated carriers can reach the SCLJ. It is also worth noting that the ~0.6 V photovoltage observed for sulfite oxidation is much lower than would be expected based on the 1.80 eV optical band gap of the material. The lack of photocurrent transients in the chopped illumination measurements presented in Figure 6a suggests that interface defect states do not dominate in limiting photovoltage in the presence of sacrificial hole acceptor. However, additional factors, such as bulk charge localization at defects and as polarons, nonoptimal electrical back contact with ITO, and limited quasi-Fermi level splitting due to rapid photocarrier recombination within the bulk, may play important roles in impeding photovoltage generation.

Stability of $\gamma$-$Cu_3V_2O_8$ under PEC conditions was tested by chronoamperometry measurements, also at an applied bias of 1.23 V versus RHE in pH 9.2 buffer but without $Na_2SO_3$ present so that stability under oxygen evolution conditions could be assessed. As can be seen in Figure 6c, the material demonstrated exceptional stability for more than 20 h. An approximately 30% increase in photocurrent density was observed over the first 3 h, which was possibly due to surface modification under operational conditions. Previously, Zhou et al.[45] carried out a systematic stability study of several CVO phases and discovered significant loss of surface V to solution after PEC tests. For Cu-rich phases, such as $\gamma$-$Cu_3V_2O_8$ and $Cu_{11}V_6O_{26}$, a Cu-rich surface oxide layer was found to prevent further V leaching from the bulk. It is possible that the same self-passivation process would enhance the OER catalytic activity of the surface and be responsible for the photocurrent density increase in the initial period of the chronoamperometry test. However, the detailed mechanism of $\gamma$-$Cu_3V_2O_8$ surface modification under illumination in aqueous solution and how the oxygen evolution rate is affected by such changes are open questions worth future investigation.

Despite the desirable bandgap and demonstrated photoactivity of $\gamma$-$Cu_3V_2O_8$, the photocurrents are very low relative to their theoretical values and the IPCE shows that photocarrier recombination dominates. To investigate the origin of this poor photocarrier extraction, we systematically studied the dependence of photocurrent on the thickness of sputtered $\gamma$-$Cu_3V_2O_8$ films under both front-side and back-side illumination. Figure 7a shows the photocurrent densities for sulfite oxidation at an applied potential of 1.23 V versus RHE measured from seven different film thicknesses. With front-side illumination, the photocurrent density initially increased with sample thickness but saturated at a thickness of 50 nm and remained unchanged for film thicknesses of up to 1.2 $\mu$m. In contrast, the back-side illuminated photocurrent densities were not only lower than their front-side counterparts, but also exhibited an exponentially decreasing trend with increasing film thickness. The reduced PEC performance of *n*-type $\gamma$-$Cu_3V_2O_8$ under back-side illumination is indicative of a short hole diffusion length. In this geometry, light absorption primarily generates charge carriers in the volume next to the back contact and the minority carriers (holes) must move toward the SCLJ. As they migrate across the film, these holes may be trapped by lattice defects and recombine with majority carriers (electrons). Therefore, in thicker films, the photogenerated holes have lower probability of reaching the surface junction. Pala et al.[46] have proposed that, in the strong absorption regime, where the film thickness $W$ is much larger than the absorption depth $\alpha^{-1}$ ($W \gg \alpha^{-1}$), the back-side illuminated photocurrent $J_{photo}$ would decay exponentially with respect to $W$, and the decay constant would be equal to the hole diffusion length $L_h$, according to


DOI: 10.1021/acs.chemmater.7b00807
Chem. Mater. 2017, 29, 3334−3345

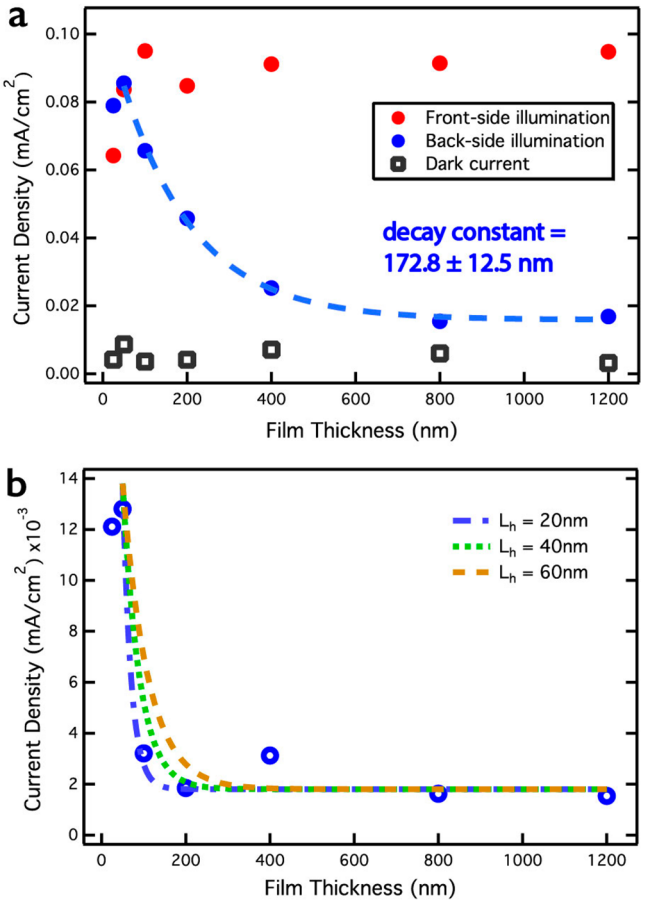


**Figure 7.** (a) Photocurrent densities under AM1.5G simulated irradiation at 1 sun intensity, with illumination from the front-side (red) and back-side (blue), as a function of film thickness. (b) Back-side illuminated photocurrent density with 340 nm irradiation. Dashed lines are the modeled photocurrent decay with 20, 40, and 60 nm hole diffusion lengths. All measurements were obtained at an applied electrochemical bias of 1.23 V versus RHE.

$$J_{\text{photo}} \propto \exp\left(-\frac{W}{L_h}\right) \tag{3}$$

Conversely, if the semiconductor were merely weakly absorbing ($\alpha^{-1} \gg W$), the back-side illuminated photocurrent would still decrease exponentially with respect to the thickness. However, the decay constant would provide a measure of the absorption depth, $\alpha^{-1}$, rather than the hole diffusion length due to the following relation:

$$J_{\text{photo}} \propto \exp(-\alpha W) \tag{4}$$

The results shown in Figure 7a were measured with a simulated solar spectrum that predominately comprises visible and infrared wavelengths. Importantly, $\gamma$-$Cu_3V_2O_8$ absorbs weakly below its 2.74 eV direct band gap, yielding absorption depths of ~0.2−2 $\mu$m in the visible range that are similar to or greater than the thicknesses of examined films. As a result, the 172.8 ± 12.5 nm decay constant obtained by fitting the back-side illuminated photocurrent densities in Figure 7a does not directly reflect the hole diffusion length but, rather, the approximate optical absorption depth. To extract the value of $L_h$, a 340 nm light-emitting diode (M340L4, ThorLabs) with ~10 nm spectral full width at half-maximum (fwhm) was used for illuminating the photoelectrodes from the back-side. Since $\gamma$-$Cu_3V_2O_8$ has much stronger absorption near 340 nm ($\alpha \approx 2.5 \times 10^5$ cm$^{-1}$, as shown in Figure 6b), this experiment falls under the strong absorption regime and can be described by eq 3. Indeed, the measured back-side illuminated photocurrent densities with a 340 nm source declined much more rapidly with thickness than the analogous measurements with the solar simulator. Using the 340 nm source, a significant drop of the photocurrent was observed between the 50 and 100 nm film thicknesses (Figure 7b). Although the available data points were not sufficient for getting a reliable fit of eq 3 for determination of $L_h$, comparison of several modeled exponential decay curves to the experimental data reveal that the hole diffusion length is in the range of 20−40 nm. Thus, it can be concluded that the PEC performance of $\gamma$-$Cu_3V_2O_8$ is limited by the poor hole transport coupled with weak light absorption ($\alpha \approx 10^3$−$10^4$ cm$^{-1}$) in the visible range.

Achieving a balance between absorption depth, $\alpha^{-1}$, and hole diffusion length, $L_h$, is known to be important for improving the extractable photocurrent. As an example, Si also absorbs visible light weakly due to its indirect band gap, but because of the exceptionally long carrier diffusion lengths in the material,[47] highly efficient light harvesting is possible from thick wafers. For materials with extremely short hole diffusion lengths, such as $\alpha$-$Fe_2O_3$ (2−4 nm),[48] it becomes crucial to facilitate carrier extraction via approaches such as elemental doping[49,50] and the decoupling of the light absorption depth from the hole diffusion length by nanostructuring.[9,10] The small optical band gap and outstanding chemical stability of $\gamma$-$Cu_3V_2O_8$ make it extremely appealing as a candidate photoanode for use in tandem PEC water-splitting cells. However, to identify its real utility, the underlying cause of the short hole diffusion length requires further investigation. In this respect, the intrinsic electronic structure and details of orbital hybridization, as studied here, can play a central role in defining carrier transport properties. Upon initial consideration, it may be expected that the Cu 3*d*-orbital character of the CBM would impose significant constraints on electron transport through highly localized and correlated states, whereas the relatively delocalized O 2*p* states of the VBM would permit relatively long hole diffusion lengths. The fact that the opposite is observed suggests that defect- or self-trapping of charge carriers plays a dominant role in defining charge extraction efficiency of the $\gamma$-$Cu_3V_2O_8$ films investigated here. While defect-related processes can be addressed via controlled growth and passivation procedures, self-trapping imposes fundamental restrictions and requires approaches such as advanced nanostructuring, composition modification, and strain engineering.

Carrier self-trapping via small polaron formation has been proposed as the major limiting factor in defining the carrier mobilities in $BiVO_4$ and a range of other transition metal oxides.[51−54] Instead of moving freely in the energy bands, photogenerated carriers localize strongly at specific lattice sites and distort the surrounding lattice, leading to slow carrier transport via thermally activated hopping. Although it has yet to be investigated in detail, charge carrier trapping and polaron formation in $\gamma$-$Cu_3V_2O_8$ are likely given the nature of this material as a charge transfer insulator. Future studies, in which DFT calculations are used for analysis of the RIXS data set, should provide additional insight into the energetic favorability of electron and hole localization. Ultimately, the degree to which hole localization effects can be overcome or managed will


DOI: 10.1021/acs.chemmater.7b00807
Chem. Mater. 2017, 29, 3334−3345

dictate whether $\gamma$-$Cu_3V_2O_8$ has actual promise as an advanced photoanode.

## 4. CONCLUSIONS

In this study, a reactive co-sputtering deposition was developed for the growth of high-quality $\gamma$-$Cu_3V_2O_8$ thin films with compact morphology and precise control of crystal phase. The indirect and direct allowed band gaps were found to be 1.80 and 2.74 eV, respectively. An additional weak absorption peak at 1.30 eV was observed and assigned to the on-site ligand field transition of $Cu^{2+}$. A comprehensive study of the electronic structure was performed with several X-ray spectroscopic techniques including XPS, XAS, nonresonant XES, and RIXS. The VBM was measured to be 1.37 eV below the Fermi energy at the vacuum interface and consist mainly of O 2*p* states, while bonding Cu 3*d* and V 3*d* states were observed to lie deeper within the valence band. The CBM was found to be dominated by unoccupied Cu 3*d* states, with V 3*d* states residing at higher energies. Together, these findings allowed the material to be classified as a charge transfer insulator with a fundamental bandgap of 1.80 eV.

The surface of $\gamma$-$Cu_3V_2O_8$ was found to possess intrinsic catalytic activity for water oxidation with ~62 $\mu A/cm^2$ photocurrent density measured at 1.23 V versus RHE under AM1.5 simulated 1 sun irradiation. In the presence of sacrificial hole acceptor, the photocurrent density was increased to 91 $\mu A/cm^2$, while the onset potential shifted cathodically to 0.70 V versus RHE. The PEC stability of $\gamma$-$Cu_3V_2O_8$ was manifested by chronoamperometric measurements that revealed stable photocurrent density, with more than 20 h of continuous operation in pH 9.2 buffer solution, possibly enabled by a self-passivation effect. Nevertheless, low IPCE values in the range of 3% were measured and indicated poor charge extraction. The limiting factor for photocurrent generation was found to be the short hole diffusion length ($L_h \approx 20-40$ nm). The finding that hole transport, rather than electron transport, is a performance limiting factor for these $\gamma$-$Cu_3V_2O_8$ photoanodes is somewhat surprising considering that the CBM comprises highly localized Cu *d*-orbital states of the upper Hubbard band, whereas the VBM is composed of O 2*p* orbitals, which should be more delocalized. Therefore, it likely that defect trapping or polaron formation plays an important role in defining carrier diffusion lengths and thus functional photoelectrode performance. These observations reveal that, while the bandgap and stability of $\gamma$-$Cu_3V_2O_8$ make it a promising candidate as a next generation photoanode material, the specific origin of the short hole diffusion length will need to be identified to determine practical limits to its efficiency for PEC applications. Furthermore, such insights are expected to inform a broader assessment of the potential of emerging transition metal vanadates as semiconductor photoelectrodes.

## ■ ASSOCIATED CONTENT

### Supporting Information

The Supporting Information is available free of charge on the ACS Publications website at DOI: 10.1021/acs.chemmater.7b00807.

XRD patterns, Raman spectrum, VASE data and fit results, Cu $2p_{3/2}$ XPS fit parameters, XAS spectra (PDF)

## ■ AUTHOR INFORMATION


### Corresponding Authors

*E-mail: JKCooper@lbl.gov.
*E-mail: IDSharp@lbl.gov. Phone: (510) 495-8715. Fax: (510) 495-8700.

### ORCID

Chang-Ming Jiang: 0000-0001-8327-5760
Cheng Hao Wu: 0000-0002-6515-0988
Jinghua Guo: 0000-0002-8576-2172
Walter S. Drisdell: 0000-0002-8693-4562
Ian D. Sharp: 0000-0001-5238-7487


### Notes

The authors declare no competing financial interest.

## ■ ACKNOWLEDGMENTS

We thank Dr. Francesca M. Toma for performing the ICP-MS measurement. This material is based upon work performed by the Joint Center for Artificial Photosynthesis, a DOE Energy Innovation Hub, supported through the Office of Science of the U.S. Department of Energy under Award No. DE-SC0004993. XAS, XES, and RIXS measurements were performed at the Advanced Light Source, which is supported by the Director, Office of Science, Office of Basic Energy Sciences, of the U.S. Department of Energy under Contract No. DE-AC02-05CH11231.

## ■ REFERENCES


(1) Toroker, M. C.; Carter, E. A. Transition Metal Oxide Alloys as Potential Solar Energy Conversion Materials. *J. Mater. Chem. A* **2013**, *1*, 2474−2484.

(2) Sun, Z.; Liao, T.; Dou, Y.; Hwang, S. M.; Park, M.-S.; Jiang, L.; Kim, J. H.; Dou, S. X. Generalized Self-Assembly of Scalable Two-Dimensional Transition Metal Oxide Nanosheets. *Nat. Commun.* **2014**, *5*, 3813.

(3) Kubacka, A.; Fernández-García, M.; Colón, G. Advanced Nanoarchitectures for Solar Photocatalytic Applications. *Chem. Rev.* **2012**, *112*, 1555−1614.

(4) Kudo, A.; Miseki, Y. Heterogeneous Photocatalyst Materials for Water Splitting. *Chem. Soc. Rev.* **2009**, *38*, 253.

(5) Sivula, K.; Le Formal, F.; Grätzel, M. Solar Water Splitting: Progress Using Hematite ($\alpha$-$Fe_2O_3$) Photoelectrodes. *ChemSusChem* **2011**, *4*, 432−449.

(6) Kim, T. W.; Choi, K.-S. Nanoporous $BiVO_4$ Photoanodes with Dual-Layer Oxygen Evolution Catalysts for Solar Water Splitting. *Science* **2014**, *343*, 990−994.

(7) Sivula, K.; van de Krol, R. Semiconducting Materials for Photoelectrochemical Energy Conversion. *Nat. Rev. Mater.* **2016**, *1*, 15010.

(8) Barroso, M.; Pendlebury, S. R.; Cowan, A. J.; Durrant, J. R. Charge Carrier Trapping, Recombination and Transfer in Hematite ($\alpha$-$Fe_2O_3$) Water Splitting Photoanodes. *Chem. Sci.* **2013**, *4*, 2724.

(9) Mohapatra, S. K.; John, S. E.; Banerjee, S.; Misra, M. Water Photooxidation by Smooth and Ultrathin $\alpha$-$Fe_2O_3$ Nanotube Arrays. *Chem. Mater.* **2009**, *21*, 3048−3055.

(10) Kim, J. Y.; Magesh, G.; Youn, D. H.; Jang, J.-W.; Kubota, J.; Domen, K.; Lee, J. S. Single-Crystalline, Wormlike Hematite Photoanodes for Efficient Solar Water Splitting. *Sci. Rep.* **2013**, *3*, 2681.

(11) Mi, Q.; Ping, Y.; Li, Y.; Cao, B.; Brunschwig, B. S.; Khalifah, P. G.; Galli, G. a; Gray, H. B.; Lewis, N. S. Thermally Stable $N_2$-Intercalated $WO_3$ Photoanodes for Water Oxidation. *J. Am. Chem. Soc.* **2012**, *134*, 18318−18324.

(12) Pihosh, Y.; Turkevych, I.; Mawatari, K.; Uemura, J.; Kazoe, Y.; Kosar, S.; Makita, K.; Sugaya, T.; Matsui, T.; Fujita, D.; et al. Photocatalytic Generation of Hydrogen by Core-Shell $WO_3$/$BiVO_4$




DOI: 10.1021/acs.chemmater.7b00807
*Chem. Mater.* 2017, 29, 3334−3345

Nanorods with Ultimate Water Splitting Efficiency. *Sci. Rep.* **2015**, *5*, 11141.
(13) Lhermitte, C. R.; Bartlett, B. M. Advancing the Chemistry of $CuWO_4$ for Photoelectrochemical Water Oxidation. *Acc. Chem. Res.* **2016**, *49*, 1121−1129.
(14) Yan, Q.; Li, G.; Newhouse, P. F.; Yu, J.; Persson, K. A.; Gregoire, J. M.; Neaton, J. B. $Mn_2V_2O_7$: An Earth Abundant Light Absorber for Solar Water Splitting. *Adv. Energy Mater.* **2015**, *5*, 1401840.
(15) Tang, D.; Rettie, A. J. E.; Mabayoje, O.; Wygant, B. R.; Lai, Y.; Liu, Y.; Mullins, C. B. Facile Growth of Porous $Fe_2V_4O_{13}$ Films for Photoelectrochemical Water Oxidation. *J. Mater. Chem. A* **2016**, *4*, 3034−3042.
(16) Dang, H. X.; Rettie, A. J. E.; Mullins, C. B. Visible-Light-Active $NiV_2O_6$ Films for Photoelectrochemical Water Oxidation. *J. Phys. Chem. C* **2015**, *119*, 14524−14531.
(17) Seabold, J. A.; Neale, N. R. All First Row Transition Metal Oxide Photoanode for Water Splitting Based on $Cu_3V_2O_8$. *Chem. Mater.* **2015**, *27*, 1005−1013.
(18) Guo, W.; Chemelewski, W. D.; Mabayoje, O.; Xiao, P.; Zhang, Y.; Mullins, C. B. Synthesis and Characterization of $CuV_2O_6$ and $Cu_2V_2O_7$: Two Photoanode Candidates for Photoelectrochemical Water Oxidation. *J. Phys. Chem. C* **2015**, *119*, 27220−27227.
(19) Zhou, L.; Yan, Q.; Shinde, A.; Guevarra, D.; Newhouse, P. F.; Becerra-Stasiewicz, N.; Chatman, S. M.; Haber, J. A.; Neaton, J. B.; Gregoire, J. M. High Throughput Discovery of Solar Fuels Photoanodes in the $CuO$-$V_2O_5$ System. *Adv. Energy Mater.* **2015**, *5*, 1500968.
(20) Kawada, T.; Ikematsu, A.; Tajiri, T.; Takeshima, S.; Machida, M. Structure and $SO_3$ Decomposition Activity of $CeVO_4/SiO_2$ Catalysts for Solar Thermochemical Water Splitting Cycles. *Int. J. Hydrogen Energy* **2015**, *40*, 10726−10733.
(21) Cooper, J. K.; Gul, S.; Toma, F. M.; Chen, L.; Liu, Y.-S.; Guo, J.; Ager, J. W.; Yano, J.; Sharp, I. D. Indirect Bandgap and Optical Properties of Monoclinic Bismuth Vanadate. *J. Phys. Chem. C* **2015**, *119*, 2969−2974.
(22) Miller, E. L.; Paluselli, D.; Marsen, B.; Rocheleau, R. E. Low-Temperature Reactively Sputtered Iron Oxide for Thin Film Devices. *Thin Solid Films* **2004**, *466*, 307−313.
(23) Koffyberg, F. P.; Benko, F. A. A Photoelectrochemical Determination of the Position of the Conduction and Valence Band Edges of P-Type CuO. *J. Appl. Phys.* **1982**, *53*, 1173−1177.
(24) Dey, S.; Ricciardo, R. A.; Cuthbert, H. L.; Woodward, P. M. Metal-to-Metal Charge Transfer in $AWO_4$ (A = Mg, Mn, Co, Ni, Cu, or Zn) Compounds with the Wolframite Structure. *Inorg. Chem.* **2014**, *53*, 4394−4399.
(25) Rakhshani, A. E.; Varghese, J. Optical Absorption Coefficient and Thickness Measurement of Electrodeposited Films of $Cu_2O$. *Phys. Status Solidi* **1987**, *101*, 479−486.
(26) Hiraga, H.; Makino, T.; Fukumura, T.; Weng, H.; Kawasaki, M. Electronic Structure of the Delafossite-Type $CuMO_2$ (M = Sc, Cr, Mn, Fe, and Co): Optical Absorption Measurements and First-Principles Calculations. *Phys. Rev. B: Condens. Matter Mater. Phys.* **2011**, *84*, 41411.
(27) Silversmit, G.; Depla, D.; Poelman, H.; Marin, G. B.; De Gryse, R. Determination of the V2p XPS Binding Energies for Different Vanadium Oxidation States ($V^{5+}$ to $V^{0+}$). *J. Electron Spectrosc. Relat. Phenom.* **2004**, *135*, 167−175.
(28) Ghijsen, J.; Tjeng, L.; van Elp, J.; Eskes, H.; Westerink, J.; Sawatzky, G.; Czyzyk, M. Electronic Structure of $Cu_2O$ and CuO. *Phys. Rev. B: Condens. Matter Mater. Phys.* **1988**, *38*, 11322−11330.
(29) Jiang, P.; Prendergast, D.; Borondics, F.; Porsgaard, S.; Giovanetti, L.; Pach, E.; Newberg, J.; Bluhm, H.; Besenbacher, F.; Salmeron, M. Experimental and Theoretical Investigation of the Electronic Structure of $Cu_2O$ and CuO Thin Films on Cu(110) Using X-Ray Photoelectron and Absorption Spectroscopy. *J. Chem. Phys.* **2013**, *138*, 24704.
(30) Biesinger, M. C.; Lau, L. W. M.; Gerson, A. R.; Smart, R. S. C. Resolving Surface Chemical States in XPS Analysis of First Row Transition Metals, Oxides and Hydroxides: Sc, Ti, V, Cu and Zn. *Appl. Surf. Sci.* **2010**, *257*, 887−898.
(31) Trześniewski, B. J.; Smith, W. A. Photocharged BiVO 4 Photoanodes for Improved Solar Water Splitting. *J. Mater. Chem. A* **2016**, *4*, 2919−2926.
(32) Cooper, J. K.; Gul, S.; Toma, F. M.; Chen, L.; Glans, P.-A.; Guo, J.; Ager, J. W.; Yano, J.; Sharp, I. D. Electronic Structure of Monoclinic $BiVO_4$. *Chem. Mater.* **2014**, *26*, 5365−5373.
(33) Olalde-Velasco, P.; Jiménez-Mier, J.; Denlinger, J. D.; Hussain, Z.; Yang, W. L. Direct Probe of Mott-Hubbard to Charge-Transfer Insulator Transition and Electronic Structure Evolution in Transition-Metal Systems. *Phys. Rev. B: Condens. Matter Mater. Phys.* **2011**, *83*, 241102.
(34) Ament, L. J. P.; Van Veenendaal, M.; Devereaux, T. P.; Hill, J. P.; Van Den Brink, J. Resonant Inelastic X-Ray Scattering Studies of Elementary Excitations. *Rev. Mod. Phys.* **2011**, *83*, 705−767.
(35) Guo, J.-H.; Butorin, S.; Wassdahl, N.; Nordgren, J.; Berastegut, P.; Johansson, L.-G. Electronic Structure of $YBa_2Cu_3O_x$ and $YBa_2Cu_4O_8$ Studied by Soft-X-Ray Absorption and Emission Spectroscopies. *Phys. Rev. B: Condens. Matter Mater. Phys.* **2000**, *61*, 9140−9144.
(36) Dong, C.; Persson, C.; Vayssieres, L.; Augustsson, a.; Schmitt, T.; Mattesini, M.; Ahuja, R.; Chang, C.; Guo, J.-H. Electronic Structure of Nanostructured ZnO from X-Ray Absorption and Emission Spectroscopy and the Local Density Approximation. *Phys. Rev. B: Condens. Matter Mater. Phys.* **2004**, *70*, 2−6.
(37) Demchenko, I. N.; Chernyshova, M.; Tyliszczak, T.; Denlinger, J. D.; Yu, K. M.; Speaks, D. T.; Hemmers, O.; Walukiewicz, W.; Derkachov, G.; Lawniczak-Jablonska, K. Electronic Structure of CdO Studied by Soft X-Ray Spectroscopy. *J. Electron Spectrosc. Relat. Phenom.* **2011**, *184*, 249−253.
(38) Strocov, V. N.; Schmitt, T.; Rubensson, J.-E.; Blaha, P.; Paskova, T.; Nilsson, P. O. Momentum Selectivity and Anisotropy Effects in the Nitrogen K-Edge Resonant Inelastic X-Ray Scattering from GaN. *Phys. Rev. B: Condens. Matter Mater. Phys.* **2005**, *72*, 85221.
(39) Gilbert, B.; Frandsen, C.; Maxey, E.; Sherman, D. Band-Gap Measurements of Bulk and Nanoscale Hematite by Soft X-Ray Spectroscopy. *Phys. Rev. B: Condens. Matter Mater. Phys.* **2009**, *79*, 35108.
(40) Eich, D.; Fuchs, O.; Groh, U.; Weinhardt, L.; Fink, R.; Umbach, E.; Heske, C.; Fleszar, a.; Hanke, W.; Gross, E.; et al. Resonant Inelastic Soft X-Ray Scattering of Be Chalcogenides. *Phys. Rev. B: Condens. Matter Mater. Phys.* **2006**, *73*, 1−6.
(41) Sharp, I. D.; Cooper, J. K.; Toma, F. M.; Buonsanti, R. Bismuth Vanadate as a Platform for Accelerating Discovery and Development of Complex Transition-Metal Oxide Photoanodes. *ACS Energy Lett.* **2017**, *2*, 139−150.
(42) Zaanen, J.; Sawatzky, G. A.; Allen, J. W. Band Gaps and Electronic Structure of Transition-Metal Compounds. *Phys. Rev. Lett.* **1985**, *55*, 418−421.
(43) Beke, S. A Review of the Growth of $V_2O_5$ Films from 1885 to 2010. *Thin Solid Films* **2011**, *519*, 1761−1771.
(44) Smith, W. A.; Sharp, I. D.; Strandwitz, N. C.; Bisquert, J. Interfacial Band-Edge Energetics for Solar Fuels Production. *Energy Environ. Sci.* **2015**, *8*, 2851−2862.
(45) Zhou, L.; Yan, Q.; Yu, J.; Jones, R. J. R.; Becerra-Stasiewicz, N.; Suram, S. K.; Shinde, A.; Guevarra, D.; Neaton, J. B.; Persson, K. A.; et al. Stability and Self-Passivation of Copper Vanadate Photoanodes under Chemical, Electrochemical, and Photoelectrochemical Operation. *Phys. Chem. Chem. Phys.* **2016**, *18*, 9349−9352.
(46) Pala, R. A.; Leenheer, A. J.; Lichterman, M.; Atwater, H. A.; Lewis, N. S. Measurement of Minority-Carrier Diffusion Lengths Using Wedge-Shaped Semiconductor Photoelectrodes. *Energy Environ. Sci.* **2014**, *7*, 3424−3430.
(47) del Alamo, J. A.; Swanson, R. M. Modelling of Minority-Carrier Transport in Heavily Doped Silicon Emitters. *Solid-State Electron.* **1987**, *30*, 1127−1136.
(48) Kennedy, J. H.; Frese, K. W. Photooxidation of Water at $\alpha$-$Fe_2O_3$ Electrodes. *J. Electrochem. Soc.* **1978**, *125*, 709−714.


DOI: 10.1021/acs.chemmater.7b00807
*Chem. Mater.* 2017, 29, 3334−3345

(49) Wang, G.; Ling, Y.; Wheeler, D. A.; George, K. E. N.; Horsley, K.; Heske, C.; Zhang, J. Z.; Li, Y. Facile Synthesis of Highly Photoactive $\alpha$-$Fe_2O_3$-Based Films for Water Oxidation. *Nano Lett.* **2011**, *11*, 3503−3509.
(50) Annamalai, A.; Lee, H. H.; Choi, S. H.; Lee, S. Y.; Gracia-Espino, E.; Subramanian, A.; Park, J.; Kong, K.; Jang, J. S. Sn/Be Sequentially Co-Doped Hematite Photoanodes for Enhanced Photoelectrochemical Water Oxidation: Effect of $Be^{2+}$ as Co-Dopant. *Sci. Rep.* **2016**, *6*, 23183.
(51) Ziwritsch, M.; Müller, S.; Hempel, H.; Unold, T.; Abdi, F. F.; van de Krol, R.; Friedrich, D.; Eichberger, R. Direct Time-Resolved Observation of Carrier Trapping and Polaron Conductivity in $BiVO_4$. *ACS Energy Lett.* **2016**, *1*, 888−894.
(52) Lany, S. Semiconducting Transition Metal Oxides. *J. Phys.: Condens. Matter* **2015**, *27*, 283203.
(53) Rettie, A. J. E.; Chemelewski, W. D.; Emin, D.; Mullins, C. B. Unravelling Small-Polaron Transport in Metal Oxide Photoelectrodes. *J. Phys. Chem. Lett.* **2016**, *7*, 471−479.
(54) Rettie, A. J. E.; Lee, H. C.; Marshall, L. G.; Lin, J. F.; Capan, C.; Lindemuth, J.; McCloy, J. S.; Zhou, J.; Bard, A. J.; Mullins, C. B. Combined Charge Carrier Transport and Photoelectrochemical Characterization of $BiVO_4$ Single Crystals: Intrinsic Behavior of a Complex Metal Oxide. *J. Am. Chem. Soc.* **2013**, *135*, 11389−11396.



DOI: 10.1021/acs.chemmater.7b00807
*Chem. Mater.* 2017, 29, 3334−3345